

Resonant Raman Intensity of the Radial Breathing Mode of Single-Walled Carbon Nanotubes within a Nonorthogonal Tight-Binding Model

Valentin N. Popov,* Luc Henrard, and Philippe Lambin

*Laboratoire de Physique du Solide, Facultés Universitaires Notre-Dame de la Paix,
61 rue de Bruxelles, B-5000 Namur, Belgium*

Received July 13, 2004; Revised Manuscript Received July 30, 2004

ABSTRACT

The resonant Raman intensity of the radial breathing mode is calculated for 50 narrow semiconducting single-walled carbon nanotubes within a symmetry-adapted nonorthogonal tight-binding model. The matrix elements of the momentum and the deformation potential in the quantum-mechanical formula for the intensity are calculated explicitly. The results for the resonance Raman profiles can be used directly in the determination of the diameter distribution of the nanotubes in a sample. Three Raman spectra are simulated and compared to existing experimental data.

Carbon nanotubes have attracted much attention of experimentalists and theorists due to their unusual vibrational, electronic, and optical properties.¹ Nanotubes can consist of a single graphitic layer (single-walled nanotubes, SWNTs) or can have a number of coaxial layers (multiwalled nanotubes, MWNTs). Nanotubes are observed either as isolated or in bundles of many tubes. The technological application of the nanotubes depends crucially on the precise characterization of the synthesized samples. Raman spectroscopy has proven to be a valuable tool for this purpose. Among the various features in the Raman spectra of nanotubes, the high-intensity band, originating from the radial breathing mode (RBM) of the nanotubes, is most often used for sample characterization.

One of the remarkable peculiarities of the Raman scattering from nanotubes is that it is observed mainly under resonant conditions, i.e., when the laser photon energy is close to an optical transition energy of a nanotube. Large-scale calculations of the transition energies were carried out within a π -band tight-binding model² and an all-valence nonorthogonal tight-binding model.³ These models do not consider self-energy and exciton effects that can lead to significant corrections to the transition energies.⁴ So far, there are no systematic calculations including both effects. Recently, extensive spectrofluorimetric data from HiPco samples⁵ of dispersed nanotubes allowed the derivation of empirical expressions for the transition energies of narrow semicon-

ducting tubes.^{5,6} Similar expressions were obtained by processing optical absorption data on HiPco samples.⁷

The successful assignment of the features in the Raman spectra requires not only the knowledge of the transition energies but also needs the dependence of the Raman intensity on the laser photon energy in the vicinity of the transition energies (so-called resonance Raman profile, RRP). Most of the quantum-mechanical simulations of the RRP use the π -band tight-binding band structure of the nanotubes and tube-independent constant matrix elements of the momentum and the deformation potential.^{8–10} In more sophisticated schemes, the matrix elements of the momentum were calculated within a π -band tight-binding model and the deformation potential was assumed to be equal to the first derivative of the transition energy with respect to the nanotube radius.^{11,12} On the experimental side, recently it has become possible to obtain well-resolved low-frequency Raman data from HiPco samples.^{13,14} The Raman spectra were assigned using the measured transition energies of ref 5 and an empirical formula for the diameter dependence of the frequency of the RBM.⁵ Although the transition energies and the RBM frequency can be predicted fairly well using empirical expressions, no empirical expressions or large-scale theoretical results exist for the RRP, which makes the determination of the diameter distribution in the nanotube samples using Raman data a challenging task.

Here we present the results of the calculations of the RRP in the RBM frequency range for 50 narrow semiconducting SWNTs. The band structure, the matrix elements of the

* Corresponding author. E-mail: valentin.popov@fundp.ac.be.

momentum, and the deformation potential, necessary for the calculation of the Raman intensity,¹⁵ are derived within a symmetry-adapted nonorthogonal tight-binding (SA-NTB) model.³ The calculated RRP of the studied tubes is approximated with a few-parameter function. The parameters of this function are tabulated and can be used for simulation of the Raman spectra of nanotube samples and for the determination of the diameter distribution of the nanotubes in the samples.

The SA-NTB has already been implemented in the calculation of the band structure and dielectric function of narrow nanotubes.³ The symmetry-adapted scheme of the model allows one to use a two-atom unit cell instead of the translational unit cell of the nanotube, which can contain thousands of atoms, and to handle practically all experimentally observed nanotubes. In this scheme, the band structure of the nanotube is obtained by solving the matrix eigenvalue equation

$$\sum_r (H_{klr'r'} - E_{kl} S_{klr'r'}) c_{klr'} = 0 \quad (1)$$

Here $H_{klr'r'}$ and $S_{klr'r'}$ are the matrix elements of the Hamiltonian and the overlap matrix elements, respectively, E_{kl} is the one-electron energy, and $c_{klr'}$ are the coefficients in the expansion of the one-electron wave function as a linear combination of the atomic orbitals of the two-atom unit cell. The one-dimensional wavevector k and the integer quantum number l are consequence of the translational and the rotational symmetries of the nanotubes ($-\pi < k < \pi, l = 0, 1, \dots, N_c - 1, N_c$ is the number of carbon pairs in the translational unit cell). The index r labels the $2n$ atomic orbitals of the two-atom unit cell ($n = 1$ for the π -band tight-binding model and $n = 4$ for the all-valence tight-binding model using $2s, 2p_x, 2p_y,$ and $2p_z$ orbitals for carbon). From eq 1, one finds the one-electron energies E_{klm} and the expansion coefficients $c_{klm'r'}$, $m = 1, 2, \dots, 2n$. For each k , this equation has to be solved for all values of l , i.e., N_c times. Therefore, the computational time for solving the eigenvalue problem for each k using standard diagonalization techniques scales as $(2n)^3 N_c$ in the symmetry-adapted scheme and as $(2nN_c)^3$ in any nonsymmetry-adapted scheme. The advantage of the former is obvious and it makes possible large-scale calculations of the Raman intensity of nanotubes where a sampling of a large number of wavevectors is required for the numerical integration over the one-dimensional Brillouin zone of the nanotube.

The quantum-mechanical description of the Raman-scattering process can be done considering the system of electrons, photons, and phonons, and their interactions.¹⁵ The most resonant Stokes process includes (a) absorption of a photon (frequency ω_L , polarization vector ϵ^L) with excitation of the electronic subsystem from the ground state with creation of an electron–hole pair, (b) scattering of the electron (hole) by a phonon (frequency ω_{ph} , polarization vector \mathbf{e}), and (c) annihilation of the electron–hole pair with emission of a photon (frequency ω_S , polarization vector ϵ^S) and return of the electronic subsystem to the ground state.

The Raman intensity for the Stokes process is given by

$$I(\omega_L, \omega_{ph}) = A \left| \sum_{\alpha\beta} \epsilon_\alpha^S \epsilon_\beta^L \sum_{i\gamma} e_{i\gamma} R_{\alpha\beta}^{i\gamma} \right|^2 \quad (2)$$

where $A \equiv C(\omega_S/\omega_L)^2(n_{ph} + 1)$, C is a tube-independent constant, and n_{ph} is the phonon thermal factor. The indices α, β , and γ run over the components of ϵ and \mathbf{e} , and the index i runs over the atoms of the two-atom unit cell. The Raman tensor $R_{\alpha\beta}^{i\gamma}$ is defined by the expression

$$R_{\alpha\beta}^{i\gamma} = \frac{1}{N} \sum_{cv} \frac{(p_\alpha)_{cv} \omega_{cv}^{i\gamma} (p_\beta)_{cv}}{(\omega_L - \omega_{cv} - i\gamma_{cv})(\omega_L - \omega_{cv} - \omega_{ph} - i\gamma_{cv})} \quad (3)$$

Here $\omega_{cv} = E_{cv}/\hbar$, E_{cv} is the vertical separation between two states in a valence band ($v = klm$) and a conduction band ($c = kl'm'$), and γ_{cv} is the excited-state width. $(p_\alpha)_{cv}$ is the matrix element of the α component of the momentum, $\omega_{cv}^{i\gamma}$ is the first derivative of ω_{cv} with respect to the γ coordinate of the i th atom, and N is the number of translational unit cells in the tube.

Here we restrict ourselves to light scattering configuration with parallel polarizations of the incident and scattered light (VV configuration). There are two particular cases of VV configurations: parallel and perpendicular ones with light polarization along and perpendicular to the tube axis, respectively. The electronic response for perpendicular VV configuration is strongly suppressed and the resulting Raman intensity is negligible. Consequently, the Raman intensity is determined from the component of the electric vector along the tube and is therefore proportional to $(\cos\varphi)^4$ where φ is the angle between the light polarization and the tube axis.¹⁶ Most often the nanotube samples consist of many tubes with random orientations and, therefore, the calculated Raman intensity should be averaged over all tube orientations. The averaging results in a constant factor multiplying the intensity for parallel VV configuration that can be combined with the existing constant C in eq 2. Consequently, the simulated Raman spectra for parallel VV configuration will be equally valid for samples with random tube orientations. These observations allow reducing the calculations for VV configurations to the case of light polarization along the tube axis when only electronic transitions $klm \rightarrow klm'$ are dipole-allowed. Additionally, because the atomic displacements of the RBM are radial, $\sum_{i\gamma} e_{i\gamma} \omega_{cv}^{i\gamma}$ is proportional to the derivative of ω_{cv} with respect to the tube radius.

First, we present the calculated RRP of the RBM for the relaxed structure of all 50 semiconducting nanotubes in the diameter range $0.56 \text{ nm} < d < 1.3 \text{ nm}$ and laser photon energies in the range $1.25 \text{ eV} < \hbar\omega_L < 1.80 \text{ eV}$. In these diameter and energy ranges fall mainly first and second transition energies, E_{ii} ($ii = 11, 22$), of semiconducting tubes. The excited-state width was taken to be $\gamma_{cv} = 0.06 \text{ eV}$ which is consistent with recent experimental data.^{12,14} The summation over the Brillouin zone in eq 3 was performed using $5000/\sqrt{N_c}$ points that are sufficient to ensure convergence of the sum. The NTB transition energies were shown to

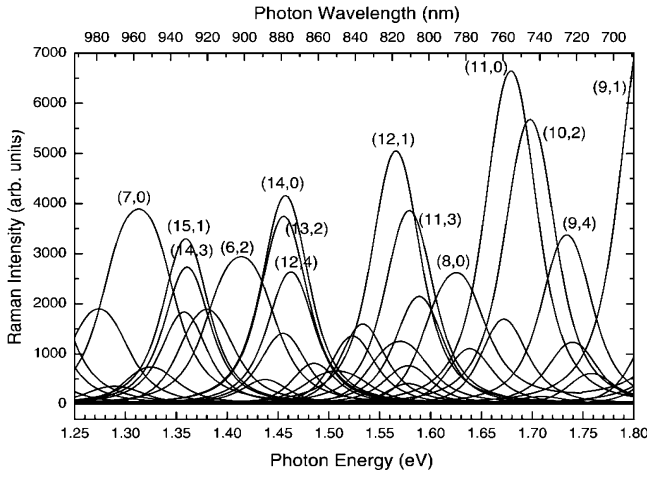


Figure 1. Calculated resonance Raman profiles of the RBM for all 50 semiconducting nanotubes in the diameter range $0.56 \text{ nm} < d < 1.3 \text{ nm}$ for the photon energy range $1.25 \text{ eV} < \hbar\omega_L < 1.80 \text{ eV}$.

underestimate the experimental data by 0.3 eV because the model does not include self-energy and exciton effects.³ On the other hand, an accuracy of a few meV is necessary for meaningful comparison with experiment, which makes the empirical relations of ref 6 preferable. For these reasons, we upshifted the calculated RRP by the difference of the transition energies E_{ii} given by the empirical relations and the NTB ones. Similarly, we estimated the RBM frequency ω_{ph} from the empirical formula⁶ $\omega_{ph} = 223.5/d + 12.5$ (ω_{ph} is in cm^{-1} and d is in nm), rather than calculating it within the NTB model. The obtained RRP of the studied tubes (per unit tube length) are shown in Figure 1. They consist of symmetric bell-like structures, each of which is formed from two broadened resonances at E_{ii} and $E_{ii} + \hbar\omega_{ph}$.

For practical reasons, it is convenient to approximate the calculated RRP with a few-parameter function. For the studied tubes, the two structures of the RRP, arising from the optical transitions with energies E_{11} and E_{22} are well separated and nonoverlapping. This fact allows approximating the two structures of each profile independently. The most suitable function can be obtained from an approximate estimation of the Raman tensor, namely, the numerator in eq 3 is assumed to be k -independent and the integration is performed analytically over the Brillouin zone of the tube.¹² The approximating function can be finally cast in the form

$$I_{ii}(\omega_L, \omega_{ph}) = \frac{1}{A|I_{ii}|} \frac{1}{\sqrt{(\omega_L - \omega_{ii} - i\gamma_{cv})^2 - (\omega_{ph}/2 - i\gamma_{cv})^2}} - \frac{1}{\sqrt{(\omega_L - \omega_{ii} - \omega_{ph} - i\gamma_{cv})^2 - (\omega_{ph}/2 - i\gamma_{cv})^2}} \quad (4)$$

where I_{ii} are parameters. If the transition energies E_{ii} and ω_{ph} are estimated from the mentioned empirical relations, I_{ii} are taken equal to $I(\omega_{ii} + \omega_{ph}/2, \omega_{ph})/A$ calculated from eq 2, and γ_{cv} is the same as above, the approximating function gives an excellent reproduction of the calculated RRP (see

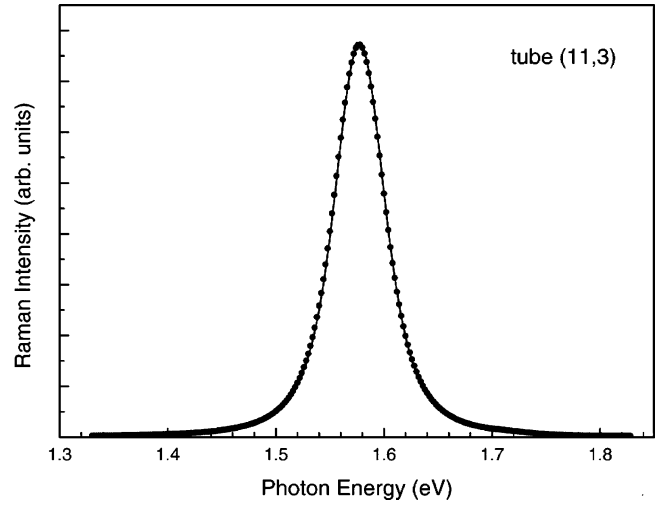


Figure 2. Calculated resonance Raman profile of the RBM of nanotube (11,3) in the vicinity of E_{22} (solid circles) in comparison with the approximated one given by eq 4 (solid line).

Figure 2). This result justifies the assumption for k -independent (but tube-dependent) numerator in the Raman tensor calculations.¹² For individual SWNTs, the intrinsic broadening γ_{cv} may be much smaller than the value used here to fit the data of ref 14 (see, e.g., ref 17). The RRP for other values of γ_{cv} is given by eq 4 with the same I_{ii} and denominator but with numerator containing the new value of γ_{cv} . The parameters I_{ii} are tabulated together with E_{ii} and ω_{ph} in Table 1. The I values do not show a clear diameter and chirality dependence, but the general trend is that tubes with smaller chiral angle and smaller diameter exhibit higher RRP. It has to be noted that these parameters have large variations for tubes with close diameters. This fact explains why some tubes were not observed (e.g., (6,4), (9,5), (10,6), (12,5), and (10,8)) and why tube (8,7) had very low intensity. Apart from this, some close-to-zigzag tube types were not observed experimentally, possibly because armchair chiralities are energetically more favorable in the HiPco growth process.⁵

Second, we used the obtained RRP to calculate the resonant Raman spectra of nanotube samples with certain diameter distributions of the tubes and for given laser photon energies. Normally, only the diameter range of the tubes in the sample is determined experimentally and the type of the diameter distribution (Gaussian, monomodal, bimodal, etc.) is unknown. Here, we considered a sample consisting of the aforementioned 50 semiconducting tubes and assumed a monomodal Gaussian distribution $g(d) = (1/\sigma\sqrt{2\pi}) \exp(-(d - d_0)^2/(2\sigma^2))$ with a mean diameter $d_0 = 0.93 \text{ nm}$ and $\sigma = 0.1 \text{ nm}$ (see ref 14). We calculated the Raman spectra of the sample for three laser photon energies using the formula

$$I_{tot}(\omega_L, \omega) = \sum g(d) I(\omega_L, \omega_{ph}) \frac{1}{(\omega - \omega_{ph})^2 + \gamma_{ph}^2} \quad (5)$$

where the summation is over the tube types. The last factor in eq 4 describes the broadening of the RBM line due to the finite phonon lifetime; the line width γ_{ph} was chosen to be

Table 1. Parameters I_{ii} (in arb. units) Together with Corresponding Optical Transition Energies E_{ii} and RBM Frequencies ω_{ph} for All 50 Nanotubes in the Diameter Range $0.56 \text{ nm} < d < 1.3 \text{ nm}$ ^a

tube (<i>n,m</i>)	<i>d</i> (nm)	θ (rad)	E_{11} (eV)	E_{22} (eV)	ω_{ph} (cm^{-1})	I_{11}	I_{22}	tube (<i>n,m</i>)	<i>d</i> (nm)	θ (rad)	E_{11} (eV)	E_{22} (eV)	ω_{ph} (cm^{-1})	I_{11}	I_{22}
(5,3)	0.556	0.380	1.721	2.374	414.7	81.58	5957	(11,3)	1.014	0.205	1.030	1.564	233.0	877.8	3863
(7,0)	0.556	0.000	1.289	3.139	414.7	3888	37120	(8,7)*	1.032	0.485	0.981	1.702	229.1	122.8	150.5
(6,2)	0.573	0.243	1.387	2.963	402.9	2941	484.0	(13,0)	1.032	0.000	0.896	1.831	229.1	1963	2024
(5,4)*	0.620	0.460	1.485	2.566	373.0	658.3	784.1	(12,2)	1.041	0.133	0.900	1.807	227.2	1718	1523
(8,0)	0.635	0.000	1.598	1.878	364.4	2622	10130	(10,5)*	1.050	0.334	0.993	1.574	225.3	282.6	2147
(7,2)	0.650	0.213	1.546	1.981	356.4	1250	7924	(11,4)*	1.068	0.260	0.905	1.740	221.8	1078	610.9
(8,1)	0.678	0.102	1.191	2.632	342.0	3223	2191	(9,7)*	1.103	0.452	0.938	1.563	215.1	11.93	764.8
(6,4)*	0.692	0.409	1.420	2.146	335.4	35.37	3415	(10,6)	1.111	0.380	0.900	1.644	213.6	443.4	50.77
(7,3)*	0.706	0.297	1.250	2.457	329.2	1899	185.9	(14,0)	1.111	0.000	0.957	1.443	213.6	1274	4159
(6,5)*	0.757	0.471	1.270	2.190	307.6	355.5	467.1	(13,2)*	1.120	0.123	0.949	1.446	212.1	1032	3743
(9,1)*	0.757	0.091	1.359	1.794	307.6	1890	7907	(12,4)*	1.145	0.243	0.924	1.450	207.7	595.5	2637
(8,3)*	0.782	0.267	1.303	1.863	298.3	736.8	5223	(14,1)	1.153	0.060	0.826	1.657	206.3	1548	1694
(10,0)	0.794	0.000	1.073	2.307	294.0	2884	2543	(9,8)*	1.170	0.490	0.879	1.533	203.6	74.16	92.15
(9,2)	0.806	0.172	1.090	2.251	289.9	2426	1402	(13,3)*	1.170	0.177	0.828	1.624	203.6	1222	1105
(7,5)	0.829	0.428	1.211	1.921	282.1	24.08	2067	(11,6)*	1.186	0.355	0.887	1.446	201.0	190.6	1408
(8,4)	0.840	0.334	1.116	2.105	278.5	1208	116.8	(12,5)	1.201	0.290	0.827	1.563	198.5	734.0	407.8
(11,0)	0.873	0.000	1.196	1.665	268.4	1776	6648	(15,1)	1.232	0.056	0.869	1.347	193.8	1058	3294
(10,2)*	0.884	0.156	1.177	1.683	265.3	1294	5677	(10,8)	1.240	0.460	0.844	1.426	192.7	9.290	487.9
(7,6)	0.895	0.479	1.107	1.914	262.3	210.8	255.9	(11,7)*	1.248	0.396	0.818	1.484	191.6	286.6	36.25
(9,4)*	0.916	0.305	1.127	1.716	256.6	435.8	3377	(14,3)	1.248	0.166	0.857	1.347	191.6	797.4	2727
(11,1)	0.916	0.075	0.980	2.032	256.6	2359	2093	(16,0)	1.270	0.000	0.764	1.521	188.5	1300	1597
(10,3)	0.936	0.222	0.993	1.963	251.3	1658	924.3	(13,5)	1.278	0.272	0.834	1.344	187.4	413.4	1837
(8,6)*	0.966	0.441	1.057	1.727	243.9	15.88	1233	(15,2)*	1.278	0.108	0.764	1.508	187.4	1179	1359
(9,5)	0.976	0.360	0.999	1.845	241.6	717.7	74.44	(14,4)*	1.300	0.213	0.764	1.472	184.4	856.9	813.1
(12,1)*	0.995	0.069	1.060	1.552	237.2	1381	5054	(10,9)	1.307	0.493	0.797	1.395	183.5	46.61	59.01

^a The quantities d and θ are the tube diameter and chiral angle, respectively. The 22 tubes tabulated in ref 14 are denoted by asterisks.

3 cm^{-1} . As seen in Figure 3, the simulated spectra are in overall agreement with the experimental spectra of ref 14. The differences are mainly in (a) the more intense peak at about 265 cm^{-1} for $\hbar\omega_L = 1.71 \text{ eV}$ and (b) the appearance of a structure between 190 and 280 cm^{-1} for $\hbar\omega_L = 1.35 \text{ eV}$ that is not present in the experimental spectrum. The origin of the former difference can be found in the possible preferred growth of tubes with close-to-armchair chirality in the HiPco process and the complete absence of zigzag tubes.⁵ We recalculated the spectra using the smaller set of 22 tubes tabulated in ref 14 and found that the obtained spectra correspond better to the measured ones than those calculated for 50 tubes (see Figure 3). Moreover, the experimental spectra suggest that there can be a bimodal diameter distribution including an additional distribution centered at $d \approx 0.75 \text{ nm}$. The consideration of the latter diameter distribution will give much higher Raman peaks for tubes (8,3) and (9,1), in agreement with experiment. We also recalculated the spectra with 22 tubes, taking a tube-independent numerator in eq 3. The obtained spectra, shown in Figure 3, differ considerably from the NTB results and the experimental data of ref 14, especially, for $\hbar\omega_L = 1.71 \text{ eV}$. Therefore, the former approximation, which is often used but was never checked so far, can lead to erroneous intensities. Finally, because the calculated and the approximated RRP (eq 4) practically coincide, the latter can be used in eq 5 to simulate any Raman spectrum very easily from the data given in Table 1. Moreover, eq 5 with the approximated RRP can be fitted to experimental Raman spectra measured at different photon energies in order to determine the actual diameter distributions of the tubes in the sample.

In conclusion, we have calculated the resonance Raman profiles of 50 narrow semiconducting tubes within a non-

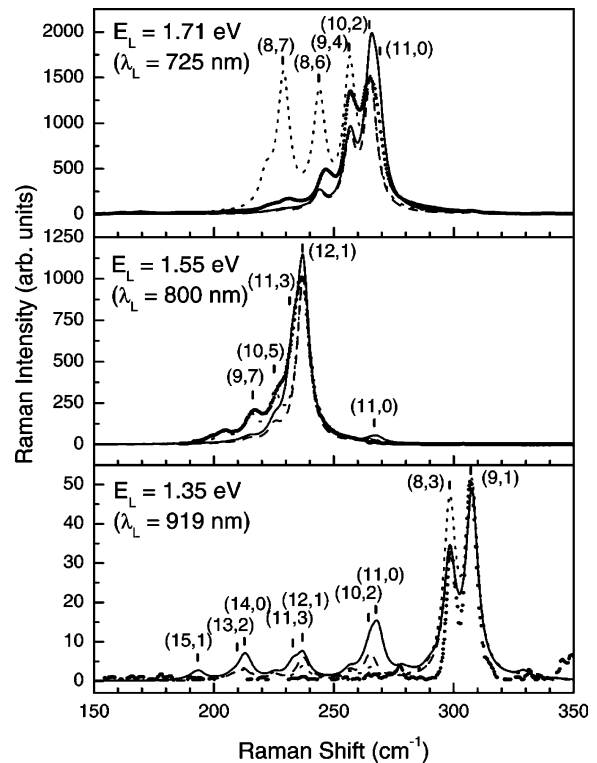


Figure 3. Calculated Raman spectra in the RBM frequency range for three photon energies for a nanotube sample with a monomodal Gaussian diameter distribution with a mean diameter $d_0 = 0.93 \text{ nm}$ and $\sigma = 0.1 \text{ nm}$. The spectra for 50 tubes (22 tubes) are drawn with solid lines (dashed lines). The spectra for tube-independent numerator in eq 3 are shown with dotted lines. The experimental data of ref 14 are given by solid circles. The spectra for tube-independent numerator and the experimental ones are normalized to have the same intensity of the highest peaks as the spectra resulting from the full calculation for 22 tubes.

orthogonal tight-binding model. The used symmetry-adapted scheme in this model allows handling practically all experimentally observed nanotubes. The proposed approximation of the derived RRP with a few-parameter function can be used for direct and fast sample characterization using Raman scattering data.

Acknowledgment. V.N.P. was partly supported by a scholarship from the Belgian Federal Science Policy Office for promoting the S&T cooperation with Central and Eastern Europe, a Marie-Curie Intra-European Fellowship MEIF-CT-2003-501080. L.H. is supported by the Belgian National Fund (FNRS). This work was partly funded by the Belgian Interuniversity Research Project on quantum size effects in nanostructured materials (PAI-UAP P5-1). V.N.P., L.H., and Ph.L. were partly supported by a NATO CLG 980422. We thank M. Strano for supplying the experimental Raman data of ref 14.

References

- (1) Dresselhaus, M. S.; Dresselhaus, G.; Avouris, Ph. *Carbon nanotubes: Synthesis, Structure, Properties, and Applications*; Springer-Verlag: Berlin, 2001.
- (2) Kataura, H.; Kumazawa, Y.; Maniwa, Y.; Umez, I.; Suzuki, S.; Ohtsuka, Y.; Achiba, Y. *Synth. Met.* **1999**, *103*, 2555–2558.
- (3) Popov, V. N. *New J. Phys.* **2004**, *6*, p. art. no.-17.
- (4) Spataru, C. D.; Ismail-Beigi, S.; Benedict, L. X.; Louie, S. G. *Phys. Rev. Lett.* **2004**, *92*, p. art. no.-077402.
- (5) Bachilo, S. M.; Strano, M. S.; Kittrell, C.; Hauge, R. H.; Smalley, R. E.; Weisman, R. B. *Science* **2002**, *298*, 2361–2366.
- (6) Weisman R. B.; Bachilo, S. M. *Nano Lett.* **2003**, *3*, 1235–1238.
- (7) Hagen A.; Hertel, T. *Nano Lett.* **2003**, *3*, 383–388.
- (8) Milnera, M.; Kürti, J.; Hulman, M.; Kuzmany, H. *Phys. Rev. Lett.* **2000**, *84*, 1324–1327.
- (9) Rafailov, P. M.; Jantoljak, H.; Thomsen, C. *Phys. Rev. B* **2000**, *61*, 16179–16182.
- (10) Jorio, A.; Souza Filho, A. G.; Dresselhaus, G.; Dresselhaus, M. S.; Saito, R.; Hafner, J. H.; Lieber, C. M.; Matinaga, F. M.; Dantas, M. S. S.; Pimenta, M. A. *Phys. Rev. B* **2001**, *63*, p. art. no.-245416.
- (11) Richter E.; Subbaswamy, K. R. *Phys. Rev. Lett.* **1997**, *79*, 2738–2741.
- (12) Canonico, M.; Adams, G. B.; Poweleit, C.; Menendez, J.; Page, J. B.; Harris, G.; van der Meulen, H. P.; Calleja, J. M.; Rubio, J. *Phys. Rev. B* **2002**, *65*, p. art. no.-201402.
- (13) Strano, M. S.; Zheng, M.; Jagota, A.; Onoa, G. B.; Heller, D. A.; Barone, P. W.; Usrey, M. L. *Nano Lett.* **2004**, *4*, 543–550.
- (14) Doorn, S. K.; Heller, D. A.; Barone, P. W.; Usrey, M. L.; Strano, M. S. *Appl. Phys. A* **2004**, *78*, 1147–1155.
- (15) Loudon, R. *Proc. R. Soc. (London)* **1963**, *275*, 218–232.
- (16) Jorio, A.; Souza Filho, A. G.; Brar, V. W.; Swan, A. K.; Ünlü, M. S.; Goldberg, B. B.; Righi, A.; Hafner, J. H.; Lieber, C. M.; Saito, R.; Dresselhaus, G.; Dresselhaus, M. S. *Phys. Rev. B* **2002**, *65*, p. art. no.-121402.
- (17) Htoon, H.; O’Connell, M. J.; Cox, P. J.; Doorn, S. K.; Klimov, V. I. *Phys. Rev. Lett.* **2004**, *93*, p. art. no.-027401.

NL048895R